Volume 13 | Number 3 | 21 January 2017 | Pages 533–696

Soft Matter

rsc.li/soft-matter-journal

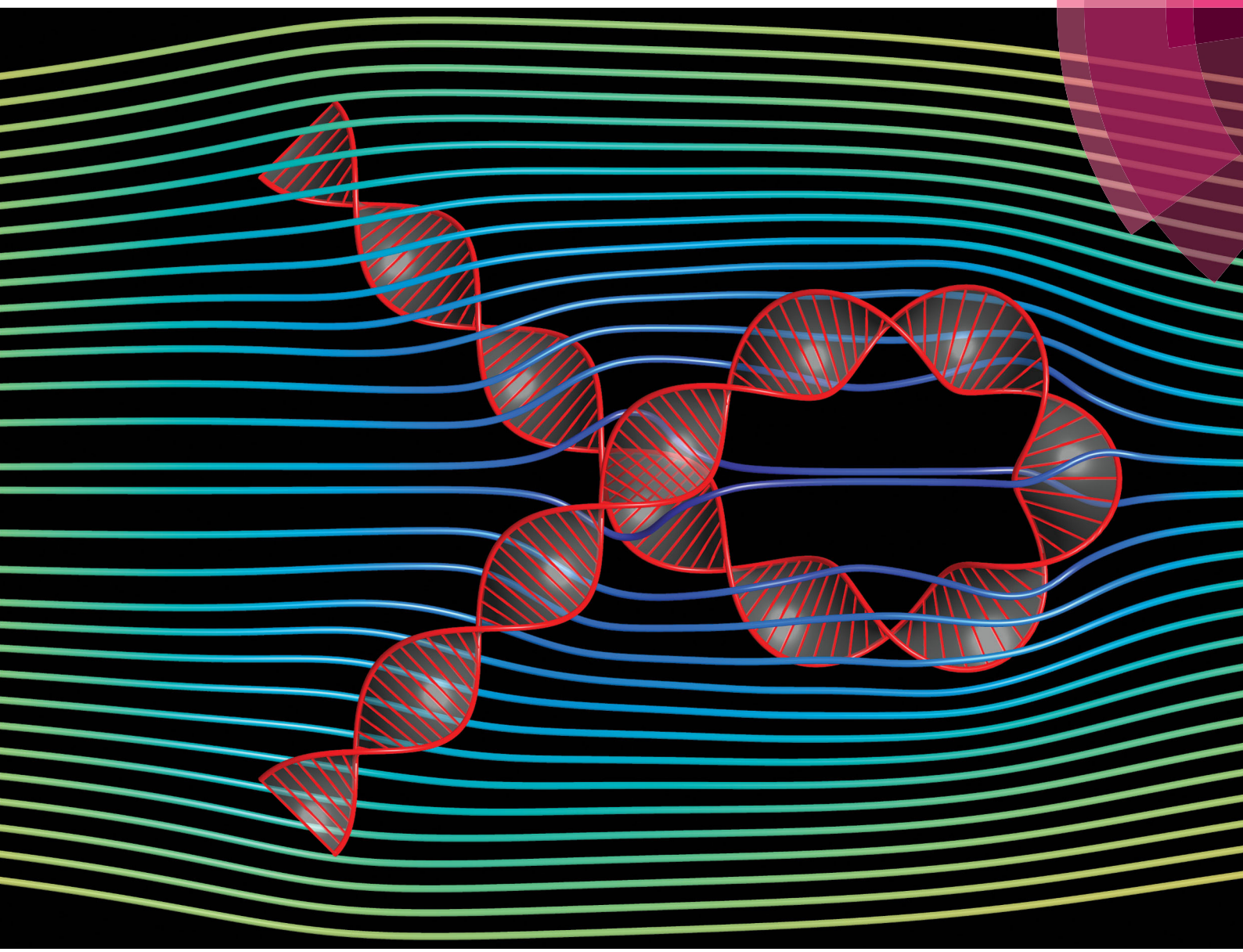

ISSN 1744-6848

ROYAL SOCIETY OF CHEMISTRY

PAPER
Thomas D. Montenegro-Johnson *et al.*
Microscale flow dynamics of ribbons and sheets

Soft Matter

PAPER

Microscale flow dynamics of ribbons and sheets

Thomas D. Montenegro-Johnson,*[ab] Lyndon Koens[b] and Eric Lauga[b]

Cite this: *Soft Matter*, 2017, **13**, 546

Received 15th September 2016,
Accepted 18th November 2016

DOI: 10.1039/c6sm02105k

www.rsc.org/softmatter

Numerical study of the hydrodynamics of thin sheets and ribbons presents difficulties associated with resolving multiple length scales. To circumvent these difficulties, asymptotic methods have been developed to describe the dynamics of slender fibres and ribbons. However, such theories entail restrictions on the shapes that can be studied, and often break down in regions where standard boundary element methods are still impractical. In this paper we develop a regularised stokeslet method for ribbons and sheets in order to bridge the gap between asymptotic and boundary element methods. The method is validated against the analytical solution for plate ellipsoids, as well as the dynamics of ribbon helices and an experimental microswimmer. We then demonstrate the versatility of this method by calculating the flow around a double helix, and the swimming dynamics of a microscale "magic carpet".

1 Introduction

At microscopic scales, fluid flow is governed by the Stokes flow equations: inertialess, and kinematically reversible.[1] The dynamics of microscale objects in Stokes flow is highly dependent upon their geometry; for example, the drag anisotropy of slender rods can cause them to translate at an angle to gravity when settling,[2] and is crucial for the swimming of microorganisms with flagellar filaments.[3,4] But for many systems of medical or industrial significance, this geometric dependence can be difficult to compute.

The Boundary Element Method (BEM)[5,6] is commonly employed in studies of microscale biofluiddynamics.[7–10] In BEM, the Stokes flow equations are transformed into an integral of Green's functions over the domain boundaries.[6] These boundaries are discretised or "meshed" into typically triangular elements (Fig. 1e), and the boundary integral is then calculated over each mesh element to form a linear system which can be solved.

However, when there is a separation of length scales in the object being studied (Fig. 1), as with for instance the slender flagellum of bacteria or spermatozoa, resolving each scale with the boundary element method can result in very large linear systems. Early work by Hancock[11] treated the slender flagellum of sea-urchin spermatozoa as a line of point forces, from which local resistive force theories were derived,[12,13] which could be generalised to any cross-sectional shape (Fig. 1b).[14] However this local treatment required the cross-sectional length scale of the filament, w, to be exponentially smaller than the centreline length, ℓ ($1 \gg 1/\log(\ell/w)$), with small curvature.

Building on this work, Slender Body Theory (SBT) was developed to determine the flow from such filaments to algebraic accuracy.[15,16] These models describe the hydrodynamics of a filament, with circular cross section, by expanding the flow from a line of point forces placed along the filament's centreline and has been used extensively to examine swimming and pumping in microscale biological systems.[17–20]

Recently, slender-ribbon theory (SRT) was developed to accurately explore the microscale hydrodynamics of slender ribbons.[21] This method expanded on the work of Johnson[16] and so captures the non-local interactions of the shape and is accurate to order w/ℓ. The slenderness condition in SRT is contingent on the assumption that all three internal length scales of the ribbon, the length, ℓ, width, w, and thickness, h, are separated $\ell \gg w \gg h$ (Fig. 1c), and the leading order flow is found by asymptotically expanding the flow from a plane of point forces representing the ribbon with respect to these length scales. The flow at the ribbon's surface is then given in terms of a line integral of unknown forces, as in SBT, which can be inverted to determine the force on the fluid. This technique allows the asymptotic exploration of a range of ribbon structures, such as artificial microswimmers comprising a magnetic head and a ribbon tail.[22–24]

While SRT captures the leading order behaviour of many ribbon shapes, it is unsuitable for highly-twisted ribbons, or those with a very curved centreline. Similarly, the asymptotic treatment of the "slender-ribbon" limit $\ell \gg w \gg h$ prevents SRT from capturing the dynamics of sheets[25] with $\ell \sim w \gg h$ (Fig. 1d), and causes the theory to break down before a standard boundary element approach becomes practical.

In this paper we develop Ribbon-BEM (RiBEM), a method to bridge the gap between SRT and BEM that is capable of solving

[a] *School of Mathematics, University of Birmingham, Edgbaston, Birmingham, B15 2TT, UK. E-mail: t.d.johnson@bham.ac.uk*
[b] *Department of Applied Mathematics and Theoretical Physics, University of Cambridge, Centre for Mathematical Sciences, Wilberforce Rd, Cambridge, CB3 0WA, UK*

This journal is © The Royal Society of Chemistry 2017

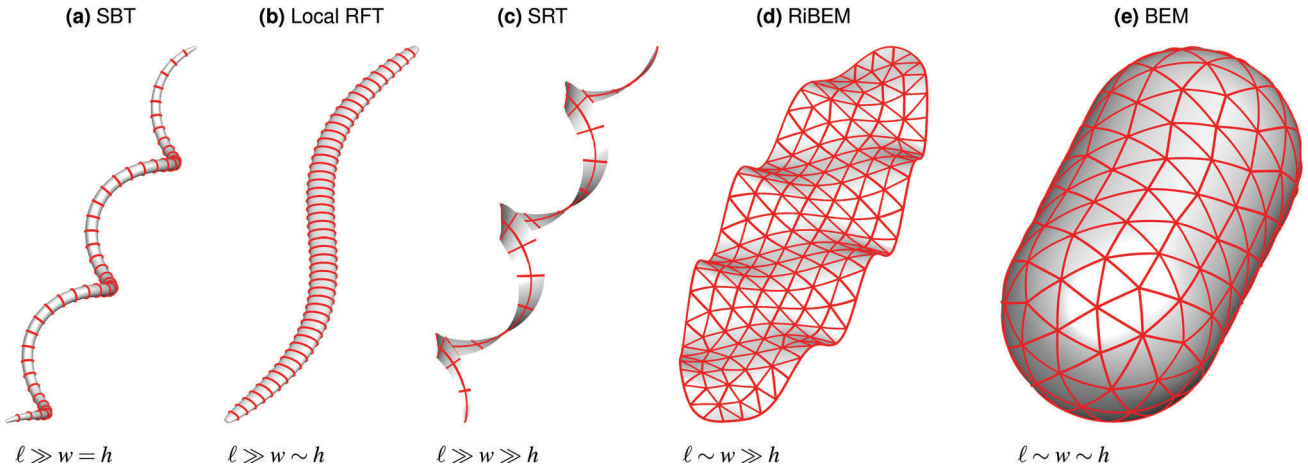

Fig. 1 Classes of shapes in Stokes flow. (a) Slender Body Theory (SBT) is an appropriate choice for long, slender bodies of circular cross-section. Examples are the flagella of bacteria or spermatozoa. (b) When this cross-section is flattened slightly, but the width and thickness are still comparable, only local drag theory (RFT) has so far been developed;[14] there is no non-local equivalent to SBT in this case, but though inefficient, boundary element methods may still be employed. An example of such a squashed slender body is the trematode worm *Schistosoma mansoni*, responsible for Schistosomiasis.[26] (c) Slender Ribbon Theory (SRT) is appropriate when all three intrinsic length scales are separated $\ell \gg w \gg h$, which can occur in artificial microswimmer design. (d) The current study sits in the domain between SRT and the Boundary Element Method (BEM) (e).

the dynamics of both highly twisted and curved ribbons as well as sheets. Inspired by previous treatments of cilia and flagella as line distributions of regularised forces[27] and SRT, we generate a two-dimensional manifold surface mesh representing the ribbon centreplane, and account for the finite thickness of the sheet *via* the regularisation parameter ε of a surface distribution of regularised forces.

The method is validated against analytical solutions for a translating plate ellipsoid, and then compared with previous BEM[28] calculations for the hydrodynamics of twisted helices and the resistance matrix of an experimental ribbon-shaped artificial microswimmer.[23] We then demonstrate the flexibility of the method by calculating the flow around a sedimenting double helix with a curved centreline, before finally considering the swimming dynamics of a finite waving sheet[25] or "magic carpet".

2 Mathematical model

We will consider microscale ribbons and sheets, for which the dynamics of the surrounding fluid is well-modelled by the Stokes flow equations

$$\mu\nabla^2\mathbf{u} - \nabla p = 0, \quad \nabla\cdot\mathbf{u} = 0, \tag{1}$$

where $\mathbf{u}$ is the fluid velocity and p the dynamic pressure.

To solve these eqn (1), we employ the regularised stokeslet boundary element method.[27,29] The velocity at a point $\mathbf{x}_0$ in the domain is given by integrals of stokeslets $\mathbf{S}$ and stresslets $\mathbf{T}$ over the swimmer surface, S,

$$\int_V u_j(\mathbf{x})\phi_\varepsilon(\mathbf{x}-\mathbf{x}_0)\mathrm{d}V_x = \int_S S^\varepsilon_{ij}(\mathbf{x},\mathbf{x}_0)f_i(\mathbf{x}) - u_i(\mathbf{x})T^\varepsilon_{ijk}(\mathbf{x},\mathbf{x}_0)n_k(\mathbf{x})\mathrm{d}S_x \tag{2}$$

for unknown surface tractions, $\mathbf{f}$, and surface velocity $\mathbf{u}$. The left-hand side is a volume integral over the fluid domain of the velocity multiplied by a 'blob' regularisation of the Dirac δ-function.

For rigid body motions, or where the volume of a swimmer is constant over its beat, we have the condition[6]

$$\int_S \mathbf{u}(\mathbf{x})\cdot\mathbf{n}(\mathbf{x})\mathrm{d}S_x = 0. \tag{3}$$

This condition also holds to a very good approximation for flexible yet inextensible swimmers provided the thickness $h \ll w, l$, since the volume of such swimmers varies only very slightly. Under condition (3), the boundary integral eqn (2) can then be rewritten in terms of a modified force density

$$u_j(\mathbf{x}_0) = \int_S S^\varepsilon_{ij}(\mathbf{x},\mathbf{x}_0)f_i(\mathbf{x})\mathrm{d}S_x, \tag{4}$$

which reduces computational complexity significantly. In our model, we will impose velocities at the depth midplane and use the regularisation to account for the finite thickness of the swimmer in a similar manner to Smith's treatment of slender bodies;[27] we thus employ the "single layer" boundary integral eqn (4). The regularisation function for the blob driving forces is given by[29]

$$\phi_\varepsilon(\mathbf{x}-\mathbf{x}_0) = \frac{15\varepsilon^4}{8\pi r_\varepsilon^7}, \quad r_\varepsilon^2 = r^2+\varepsilon^2, \tag{5}$$

where $r_i = (\mathbf{x}-\mathbf{x}_0)_i$, $r = |\mathbf{x}-\mathbf{x}_0|$ and $\varepsilon \ll 1$. For such a blob force, the regularised stokeslet is then

$$S^\varepsilon_{ij}(\mathbf{x},\mathbf{x}_0) = \frac{\delta_{ij}\left(r^2+2\varepsilon^2\right)+r_ir_j}{8\pi r_\varepsilon^3}. \tag{6}$$

We will discretise the boundary integral eqn (4) over mesh of geometrically piecewise-quadratic triangles. The unknown tractions $\mathbf{f}$ will be discretised as piecewise-constant $f_i[1],\ldots,f_i[N]$ over each element $E[1],\ldots,E[N]$, where $E = E[1]\cup\ldots\cup E[N]$ is the

surface mesh of N elements describing the ribbon or sheet. This discretisation yields a matrix system of the form

$$u_j(\mathbf{x}_0) = \sum_{n=1}^{N} f_i[n] \int_{E[n]} S_{ij}^{\varepsilon}(\mathbf{x}, \mathbf{x}_0) \mathrm{d}S_x, \quad \mathbf{x}_0 \in E[m], \tag{7}$$

where $\mathbf{x}_0$ is the centroid of element $E[m]$, with $m = 1,\ldots, N$ and $i, j = 1, 2, 3$. This yields $3N$ equations for the $3N$ unknown surface tractions. Element integrals of the regularised stokeslets are performed using adaptive Fekete quadrature. Code is implemented in matlab, and adapted from the authors' previous work.[30] We will now proceed with a validation of this method against previous analytical and numerical results.

3 Validation

3.1 Plate ellipsoids

We begin by considering the resistance of a plate ellipsoid to the 6 principal translations and rotations. The total drag F on an ellipsoid with semi-axes $\{\ell,w,h\}$, where without loss of generality $\ell \geq w \geq h$, translating at speed U in direction ℓ is given by[31]

$$\frac{F}{\pi\mu U} = \frac{16}{\phi + \zeta_\ell \ell^2}, \tag{8}$$

while the torque T due to a rotation at rate Ω about ℓ is given by

$$\frac{T}{\pi\mu\Omega} = \frac{16}{3} \frac{w^2 + h^2}{w^2\zeta_w + h^2\zeta_h}, \tag{9}$$

where

$$\phi = \int_0^\infty \frac{\mathrm{d}x}{\sqrt{(\ell^2 + x)(w^2 + x)(h^2 + x)}}, \tag{10a}$$

$$\zeta_\ell = \int_0^\infty \frac{\mathrm{d}x}{(\ell^2 + x)\sqrt{(\ell^2 + x)(w^2 + x)(h^2 + x)}}, \tag{10b}$$

$$\zeta_w = \int_0^\infty \frac{\mathrm{d}x}{(w^2 + x)\sqrt{(\ell^2 + x)(w^2 + x)(h^2 + x)}}, \tag{10c}$$

$$\zeta_h = \int_0^\infty \frac{\mathrm{d}x}{(h^2 + x)\sqrt{(\ell^2 + x)(w^2 + x)(h^2 + x)}}. \tag{10d}$$

The regularisation ε is chosen such that the thickness of the semi-axis $h = \varepsilon$, in the same way that ε is used as a proxy for filament thickness in regularised stokeslet slender body theory.[27] In practice, provided ℓ, $w \gg h$, the drag is fairly insensitive to this choice; substituting values of $\ell = 1$, $w = 0.1$ then $h = 0.001$, 0.0005 into the above equations, we see less than a 0.3% difference in all 6 components of the resistance matrix. Note that since we keep the regularisation constant over the entire surface, our model in fact represents an elliptical disk of finite thickness. Nonetheless, for very thin discs, we expect this discrepancy to be small.

Fig. 2a shows a particular drag component, the broadside drag F_h, on a thin plate ellipsoid of semi-axis length $\ell = 1$ and thickness $h = 0.005$ as a function of varying width w. The analytical solution is compared to numerical solutions calculated

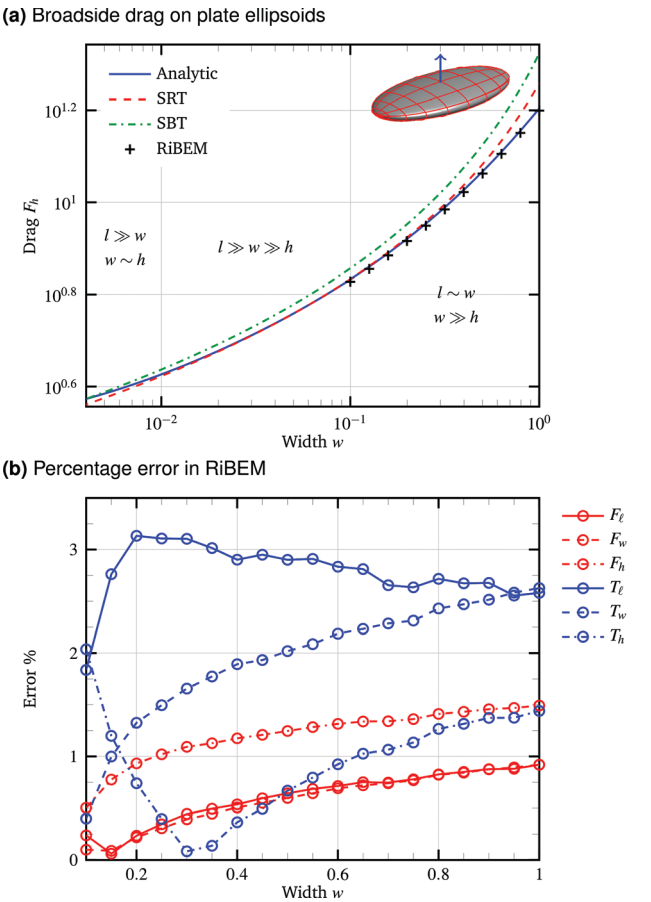

Fig. 2 (a) Comparing methods of evaluating the broadside drag (direction demonstrated on the inset ellipsoid) F_h on a plate ellipsoid of length $\ell = 1$, thickness $h = 0.005$, and varying width w. RiBEM performs well until $w \sim 0.1$ in a region roughly corresponding to Fig. 1d, whereafter it because difficult to resolve meshes. SRT is thereafter very accurate for this component in the region corresponding to Fig. 1c, but is finally superseded by SBT once width and thickness are comparable (the region of Fig. 1b). At the bottom of the range, $w = h = 0.005$ and SBT gives the drag exactly. (b) The percentage error in the principal components of the resistance matrix as calculated by RiBEM for slightly thicker plate ellipsoids with $\ell = 1$, $h = 0.01$ and varying w, showing good agreement with analytical results.

via RiBEM, SRT, and SBT assuming the radius of the filament is given by w. The RiBEM meshes for ellipse-based geometries are generated using routines adapted from DistMesh,[32] with a desired uniform mesh element edge length dependent upon the area of the ellipse, $A = \pi\ell w$, so that $E_l = \sqrt{\pi\ell w/500}$. Since an ideal mesh comprises equilateral triangles, which have an area $A_t = \sqrt{3}E_l^2/4 \approx E_l^2/2$, this choice results in uniform meshes with approximately $N = 1000$ elements for each value of width w.

In the region $1 \geq w \geq 0.3$, $\ell \sim w \gg h$, and the geometry is a sheet as in Fig. 1d. RiBEM performs very favourably in this régime, while the asymptotic solutions of SRT and SBT significantly overestimate the drag. As w decreases, we begin to separate all three length scales $\ell \gg w \gg h$ (Fig. 1c), and for $0.3 \geq w \geq 0.1$, SRT has a similarly high accuracy to RiBEM, whereas SBT is still significantly off. At around $w = 0.1$, $\ell \gg w$, and it becomes increasingly difficult to numerically resolve the

 This journal is © The Royal Society of Chemistry 2017

geometry using RiBEM, as retaining resolution in the w direction leads to a very fine mesh in the ℓ direction. This results in large matrix systems with RiBEM, and so SRT becomes the appropriate choice. At around $w = 0.01 \sim h$, we no longer have separation of scales between the width and thickness $\ell \gg w \sim h$ and the slender ribbon assumption is no-longer valid. In this régime, (Fig. 1a and b) SBT becomes the current most accurate choice, finally recovering the drag exactly when $w = 0.005 = h$. These results demonstrate the need to choose the correct method based on the separation of length scales in the geometry being considered, as shown in Fig. 1.

In Fig. 2b, we validate RiBEM for all 6 values of the resistance matrix for a thicker ellipsoid with $\ell = 1$, $h = 0.01$, and $w \in [1,0.1]$. Finding all 6 diagonal values of the resistance matrix with approximately $N = 1000$ elements took approximately 15 seconds for each value of w on a Dell Optiplex 9020 desktop computer. Even for this relatively coarse discretisation, the error in the mobility tensor is small, less than 3% for all components.

3.2 Helical ribbons

Recently, Keaveny and Shelley[28] explored how a helical ribbon's configuration and aspect ratio, h/w, changed its propulsive capability. This investigation used a boundary element method and considered ribbons with an ellipsoidal cross-section and the parametrisation

$$\mathbf{r}(s_1) = \{r_h \cos(ks_1), r_h \sin(ks_1), \alpha s_1\}, \quad (11)$$

$$\hat{\mathbf{T}}(s_1) = \cos(\gamma)\hat{\mathbf{b}} - \sin(\gamma)\hat{\mathbf{n}}. \quad (12)$$

Here, $\mathbf{r}(s_1)$ is the helix centreline, r_h is the helix radius, $k = 4\pi$ is the helix wavenumber, and α is the cosine of the helix angle. The unit vector $\hat{\mathbf{T}}(s_1)$ points towards the major axis of the ribbon cross-section, while γ is the angle between the helix axis and $\hat{\mathbf{T}}$. Finally, $\hat{\mathbf{n}}$ and $\hat{\mathbf{b}}$ are the normal and binormal vectors to the helix centreline. Fig. 3a shows two example ribbons generated by this parameterisation.

The thinnest of the ribbons considered by Keaveny and Shelley,[28] with $h/w = 1/4$, lie at the borderline where traditional boundary element techniques can become computationally infeasible. However, at these aspect ratios or finer, RiBEM is an effective alternative. Fig. 3b shows the effect of varying $0 \leq \gamma \leq \pi/2$ on configurations with $\alpha = 0.5$, 0.75 and 0.9, with $h/w = 1/4$ for Keaveny and Shelley's results with an ellipsoidal cross-section compared with RiBEM results for $\varepsilon/w = 1/5$ for a rectangular cross-section; this aspect ratio is chosen such that the rectangular cross section $4hw \approx \pi hw$ the ellipsoidal cross-section, as $\pi/16 = 0.196 \approx 1/5$. These results are in very good agreement, indicating that even for relatively thick ribbons, this choice of $\varepsilon = h$ provides a reasonable proxy for finite thickness with small deviations arising from the difference in cross-sectional shape, which reduce for thinner ribbons. Indeed, it should be noted that for manufacturing purposes, a rectangular cross-section may in fact be preferable, as in the following case.

3.3 A magnetic microhelix

Helical ribbons, similar to those considered above, have recently been used in laboratory settings to create artificial bacterial flagella

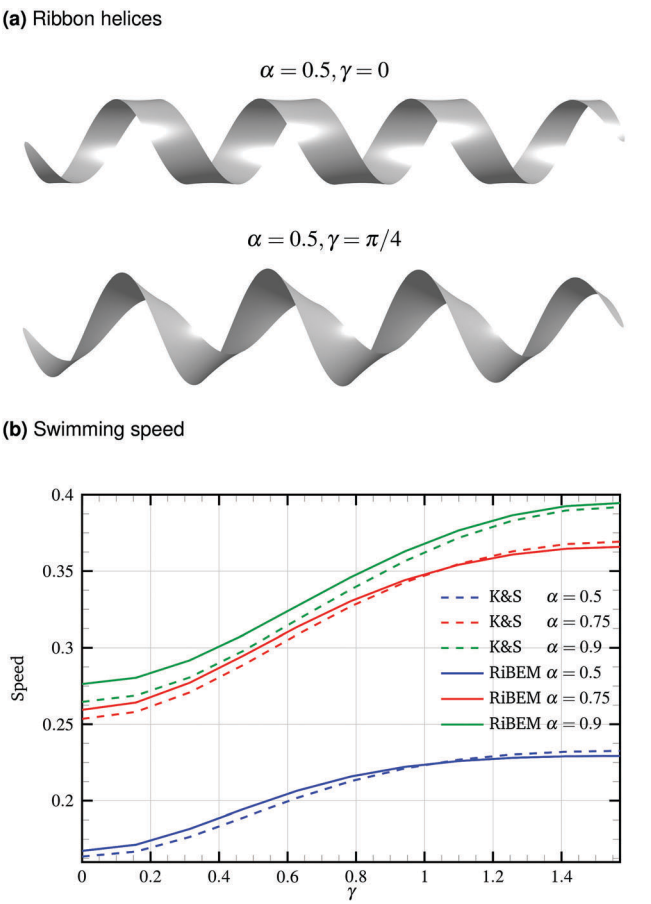

Fig. 3 The dynamics of helical ribbons. (a) Ribbons given by the parameterisation eqn (11) and (12) with $\alpha = 0.5$, and $\gamma = 0$ (left) and $\gamma = \pi/4$ (right). (b) The swimming velocity in response to a unit torque about the helix axis for varying γ. The dashed lines are the results of Keaveny and Shelly[28] for ribbons with $h/w = 1/4$, while the solid lines are the results from RiBEM for ribbons with $\varepsilon/w = 1/5$. The slight discrepancy between these results is likely because the Keaveny results have an elliptical cross-section, where as the RiBEM results are for a flat cross-section.

(ABF).[23] These ABFs comprise a magnetic head rigidly attached to a helical ribbon tail, and swim when driven by an external rotating magnetic field. The swimming behaviour has in turn been used to experimentally determine the resistance coefficients of such a swimmer,[23] which have also been analysed theoretically using SRT[21] and BEM.[33] The flexibility of RiBEM allows us generate a realistic computational mesh of the experimental system (Fig. 4). Indeed, provided that the geometric condition $\ell/h, w/h \gtrsim 5$ holds, the approximate borderline as above between RiBEM and BEM, RiBEM will be an effective method for the computational design and optimisation of low Reynolds number artificial swimmers with ribbon or sheet-like geometries.

In the SRT study of this ABF, the ribbon was treated as asymptotically thin, with the head modelled as a plate ellipsoid without non-local hydrodynamic interactions. In the BEM study, the aspect ratio of $h/w = 1/4$ overestimated the ribbon thickness by an order of magnitude. We now attempt to use our model in order to resolve differences between the previous studies and the experimental data.

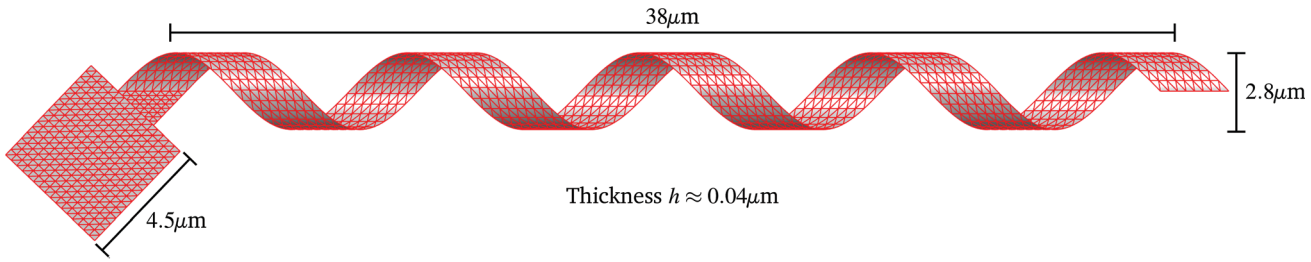

Fig. 4 Computational mesh of the magnetic helical microswimmer studied in ref. 23 Note that this mesh differs from previous numerical studies as the edges of the ribbon are not curved and the head is not approximated by an ellipsoid, however these differences do not have much of an effect on the resistance matrix, with the present study agreeing with previous treatments using BEM for a significantly fatter mesh and SRT.

The experimental ABF considered had a slender ribbon tail with an axial length of L = 38 μm, width w = 1.8 μm, and thickness h = 42 nm, and a square magnetic head with dimensions of 4.5 μm × 4.5 μm × 200 nm. The ribbon was helical, as a ribbon wrapped around a pencil, and had a helix diameter of $2r_h$ = 2.8 μm immediately after fabrication. We therefore describe this ribbon using eqn (11), but with $\hat{\mathbf{T}} = \hat{\mathbf{z}}$, where $\hat{\mathbf{z}}$ is the helix axis. The mesh used for the RiBEM calculations, generated using simple custom routines, is shown in Fig. 4. This mesh is closer to the experimental system than those used in previous studies,[21,33] since it does not exhibit the curved edges, which are not present in the experiment, found from the ribbon parameterisation based upon eqn (11) and (12).

Table 1 lists the experimentally-determined resistance coefficients and the corresponding resistance coefficients of each model. Significantly, we see that all independent theoretical models predict similar values for the resistance coefficients, with slight variations likely due to the details of each model. This result would seem to indicate that the discrepancy was not caused by the approximations present in the previous SRT or BEM studies. The drag coefficient R_a is underpredicted in all models, while the coefficient coupling axial rotation and translation R_b is best captured using the boundary element method or the RiBEM code. The rotational coefficient R_c is overestimated significantly by all three models. Koens and Lauga[21] hypothesised that the curved edge of the SRT/Keaveny parameterisation might be responsible for this discrepancy. However, since this approximation is not present in our RiBEM model, the source of this discrepancy remains unclear.

Table 1 Hydrodynamic resistance coefficients for the ribbon microswimmer. Left: Experimental measurements.[23] Middle-left: SRT results assuming $2r_h$ = 2.8 μm.[21] Middle-right: The BEM model swimmer results from ref. 33 Right: RiBEM result assuming $2r_h$ = 2.8 μm. The hydrodynamic resistance coefficient R_a relates the drag force experienced parallel to the helical axis from translation in the same direction, whereas R_b is the hydrodynamic force experienced parallel to the helix axis from rotation around the helix axis, and R_c is the hydrodynamic torque experienced around the helical axis from rotation around said axis of both the head and the helix

	Exp.	SRT	BEM	RiBEM
R_a (10^{-7} N s m^{-1})	1.5	1.04	0.937	0.932
R_b (10^{-14} N s)	−1.6	−1.32	−1.63	−1.47
R_c (10^{-19} N m s)	2.3	6.81	10.1	9.91

4 Results

4.1 A coiled double helix

The helix above is an experimental realisation of the bacterial flagellum: a microscale chiral structure that couples rotation with translation. In the example above, the centreline of the helix is twisted about a central axis, but the ribbon itself is not twisted about its centreline. Centreline twist is another fundamental chirality which can couple rotation and translation, and is observed in nature in, for instance, the double helix of DNA.

In order to demonstrate the simplicity and flexibility of our method, we now calculate the 6 × 6 Grand Resistance Matrix (GRM) of a rigid, coiled double helix, and the streamlines resulting from uniform flow past it. The centreline we prescribe for the double helix is given by two straight lines, folding over into the lemniscate of Bernoulli, given by the parametric equation

$$x = \frac{\sqrt{2}\cos t}{\sin^2 t + 1}, \quad x = \frac{\pm(t \pm \pi/2)}{\sqrt{2}}, \tag{13a}$$

$$y = \frac{\sqrt{2}\sin t \cos t}{\sin^2 t + 1}, \quad y = \frac{t \pm \pi/2}{\sqrt{2}}, \tag{13b}$$

$$t \in (-\pi/2, \pi/2),\ t \in [-\pi, -\pi/2], \quad t \in [\pi/2, \pi], \tag{13c}$$

with $z = 0.1t$, $t \in [-\pi, \pi]$. We generate constant twist along this centreline, with $\hat{\mathbf{T}} = \cos(2\pi ks/L)\hat{\mathbf{b}} + \sin(2\pi ks/L)\hat{\mathbf{n}}$ for centreline binormal $\hat{\mathbf{b}}$ and normal $\hat{\mathbf{n}}$. Here, we denote the arclength of the centreline by s, which differs from the parametric variable t, the length of the centreline L, and the wavenumber k = 6. This parametrisation, with a width of $w = L/20$, produces the folded double helix shown in Fig. 5.

Setting an arbitrary small thickness of $h = 0.01 \approx w/35$, the resistance matrix for the double helix in this configuration, with a resolution of N = 3200 elements, is given by

$$\begin{bmatrix} 13.0274 & 0.0002 & -0.0002 & 0.1688 & -0.0017 & -0.0017 \\ 0.0002 & 14.0480 & 0.2342 & 0.0004 & -0.1690 & 0.2704 \\ -0.0002 & 0.2343 & 16.3583 & 0.0008 & -1.4422 & 0.2710 \\ -0.1688 & 0.0005 & 0.0009 & 11.8006 & 0.0008 & 0.0005 \\ -0.0015 & -0.1693 & -1.4422 & 0.0004 & 21.0341 & 1.9619 \\ -0.0018 & 0.2704 & 0.2706 & 0.0005 & 1.9623 & 24.4865 \end{bmatrix}$$

This journal is © The Royal Society of Chemistry 2017

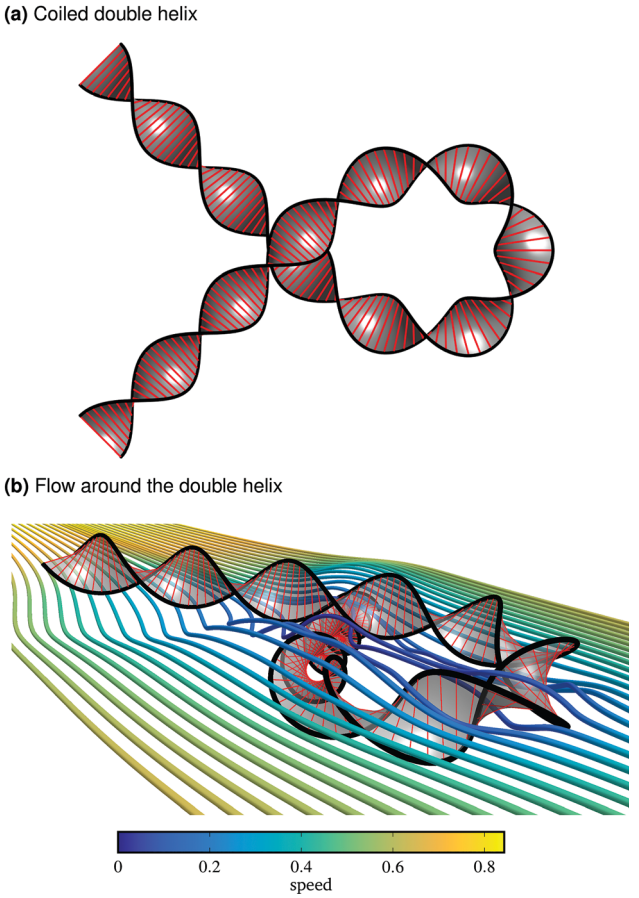

Fig. 5 (a) Plan view of a double helix with straight ends, coiled over into a half figure-of-eight. (b) Uniform flow past the double helix, showing streamlines that are deflected as though by an equivalent cylinder, and a few streamlines that follow the twisting surface more closely.

It is worth noting that this is remarkably similar to the resistance matrix of a cylinder extruded along the same centre-line, capped by hemispheres, with radius $w = L/40$ (*i.e.* half the radius of the ribbon)

$$\begin{bmatrix} 12.7157 & -0.0000 & 0.0000 & 0.1716 & 0.0000 & 0.0000 \\ 0.0000 & 13.6380 & 0.2477 & 0.0000 & 0.0891 & -0.3409 \\ 0.0000 & 0.2476 & 16.0148 & -0.0000 & -1.9322 & -0.2118 \\ 0.1716 & 0.0000 & 0.0000 & 11.5256 & 0.0000 & 0.0000 \\ -0.0000 & 0.0891 & -0.9325 & -0.0000 & 20.2099 & 2.2285 \\ -0.0000 & -0.3407 & -0.2120 & 0.0000 & 2.2281 & 24.4529 \end{bmatrix}$$

with only some very small off-diagonal elements arising from the twisting of the helix not present. This supports previous observations[21] that the GRM of a double helix is well-modelled by an "average" cylinder. We note however that three of the terms in the DNA coupling sub-matrix have the opposite sign to the cylinder case. This change in sign is due to the twisting of the ribbon's surface creating a different flow pattern. However as these terms are two orders of magnitude smaller than the largest terms in the GRM, only very accurate experiments will be able to measure them.

The GRM only captures the trajectories of rigid objects, and does not account for detailed flow structures at the ribbon surface or the spatially-dependent force per unit area on the structure. Instantaneous flow streamlines for a sedimenting double helix in the frame in which the body is stationary are shown in Fig. 5b, revealing intricate patterns and twisting streamlines near the surface. A particularly interesting avenue of future research will be to couple this fully-resolved flow and surface tractions to a constitutive model for the double helix itself. Omori *et al.*[34] modelled the deformation of a red blood cell, a closed membrane travelling through a micropore, by coupling the standard boundary element method for flow to a finite element solution for a thin hyperelastic membrane representing the cell. Finite element shell computations for open membranes could be coupled to RiBEM in an analogous way, indeed the flexibility of regularised stokeslet methods makes them ideal for coupling with elastic models for structures.[35]

4.2 Taylor's magic carpet

G. I. Taylor's model of a small-amplitude, infinite swimming sheet[36] is often used as an analytical means to study microscale propulsion, and is increasingly being used to examine swimming in non-Newtonian fluids.[37,38] Furthermore, a finite-sized analogue of Taylor's sheet has recently been developed experimentally,[25] driven by an applied magnetic field as a means of achieving controlled locomotion at small scales.

Our method allows us to model a range of plate microswimmers exhibiting different dynamics. We consider an inextensible plate ellipsoid of length $L = 1$, thickness $h = 0.005$, and variable width w, propagating bending waves along its length. Let $s = [0,1]$ be the length coordinate relative to the head of the swimmer in an undeformed configuration, and $r = [-w/2, w/2]$ the width coordinate. We model planar beating in the length x- and thickness z-plane, so that the tangent angle of the swimmer surface in this plane is

$$\psi(s,t) = As^{1/2}\cos 2\pi(ks - t), \tag{14}$$

giving body-frame surface coordinates

$$x = \int_0^1 \cos(\psi(s,t))\mathrm{d}s, \quad z = \int_0^1 \sin(\psi(s,t))\mathrm{d}s, \quad y = r, \tag{15}$$

and body-frame velocity

$$u = \int_0^1 -\dot{\psi}\sin(\psi(s,t))\mathrm{d}s, \quad w = \int_0^1 \dot{\psi}\cos(\psi(s,t))\mathrm{d}s, \quad v = 0. \tag{16}$$

This parameterisation results in the beat pattern shown in Fig. 6a. The two unknown swimming x and z translational velocities and the rotational velocity about the y-axis are found by enforcing the constraints that the swimmer is force and torque free

$$\int_S \mathbf{f}(\mathbf{x},\mathbf{t})\mathrm{d}S_x = \mathbf{0}, \quad \int_S \mathbf{x}\wedge\mathbf{f}(\mathbf{x},\mathbf{t})\mathrm{d}S_x = \mathbf{0}, \tag{17}$$

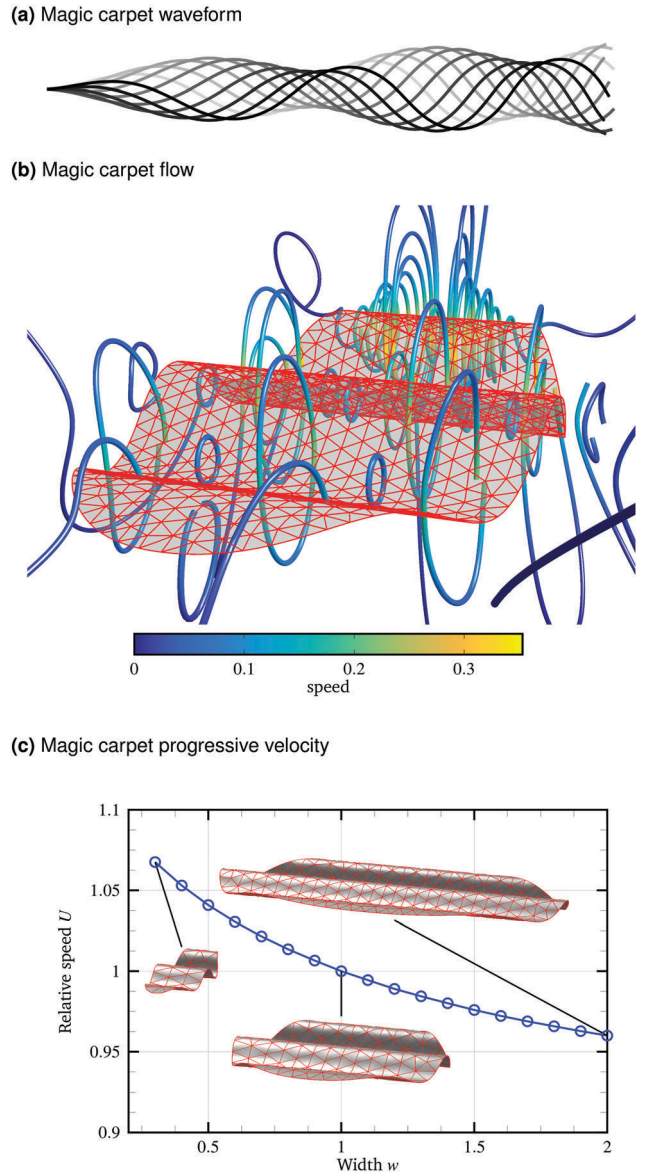

Fig. 6 (a) Grayscale time-lapse of the planar waveform of the magic carpet as defined by the tangent angle (19). (b) Flow streamlines driven by a magic carpet with $w = L/2$, $k = 5\pi/2$, and $A = \pi/3$ at time $t = 0$, demonstrating similar vortices to those observed in 2D and 3D analogues. (c) Swimming velocity of the magic carpet relative to a circular disk, demonstrating that for finite swimmers, slender filament configurations are faster than wide carpets exhibiting the same beat kinematics.

and the sheet's mean progressive velocity determined from its laboratory frame trajectory.[17]

An instantaneous configuration of a swimmer with $w = 0.5$, $k = 5\pi/2$, and $A = \pi/3$ at time $t = 0$ is shown in Fig. 6b, together with the resultant flow streamlines, in the laboratory frame. The streamlines reveal an intricate pattern of recirculating vortices at the swimmer surface, as observed both with filament swimmers and in two-dimensional (2D) infinite sheet models; this intermediate model retains many of the flow features of both limits.

We might also ask how the mean progressive velocity of such a swimmer varies with width. Fig. 6c shows the progressive velocity of this sheet swimmer as the width varies from $w = 0.3, \ldots, 2$ relative to the circular disk configuration. For the range considered, slender ribbons exhibiting the same kinematics swim more quickly than broader swimmers. The hydrodynamic mechanism for this reduction for these parameters can, somewhat crudely, be understood in the following manner. The propulsive force that the sheet exerts on the fluid is approximately proportional to the area of the ellipse, which scales with w. The drag in the swimming direction can be approximated by F_ℓ (8). The swimming velocity is then such that drag and propulsion balance exactly, since the swimmer is force-free. However, we can observe through simple numerical evaluation of the integrals (10) that the drag force (8) increases more rapidly with width than the surface area in this régime; thus for an increase $\mathrm{d}w$ in width, the increase in drag $\mathrm{d}D > \mathrm{d}F$ the increase in propulsion, and the swimmer moves more slowly.

It is interesting to ask if the increase in velocity continues as the width decreases further. By modelling the swimmer centreline by a line distribution of 3D regularised stokeslets, we obtained a relative swimming speed for the filament of $U = 1.032$. This result suggests that there may exist an optimal cross-section which produces the fastest swimming speed in the nearly filament régime (Fig. 1b) where there is currently no non-local theory, providing further motivation for its development. However, it is important to note that the regularised stokeslet slender body theory is a different method for simulating fundamentally different geometries; whilst the relative error between two RiBEM solutions for similar geometries will be small, the absolute accuracy of RiBEM is around 3% (Fig. 2), and as such further study in the nearly filament régime is required to verify the existence of this optimum.

We again note that RiBEM would be highly suited for future coupling with a shell theory that incorporates elastic bending in order to study actively bending plate swimmers, in an analogous manner to previous work with sperm-like flagellar swimmers.[39]

5 Discussion

We have demonstrated that the boundary element method with regularised stokeslets is an effective means of calculating the dynamics of thin ribbons and sheets, where the regularisation parameter ε is used as a proxy for the sheet thickness. Tractions are not resolved across the thickness of the sheet, but rather regularised stokeslets are distributed across a 2D manifold of the ribbon's centreline. The method is accurate in regions where asymptotic theories are not valid, and traditional boundary elements are impractical.

The method was validated against the analytical solution for the resistance matrices of various plate ellipsoids as well as previous boundary element studies of ribbon helices, and shown to be consistent with asymptotic and boundary element studies of an experimental ribbon microswimmer. We then applied the method to study the resistance and flow surrounding a coiled section of double helix, finding that whilst the

 This journal is © The Royal Society of Chemistry 2017

resistance matrix was very similar to an equivalent cylinder, the flow streamlines showed an interesting structure which would be important to resolve in fluid-structure interaction models. We finally examined an inextensible, finite plate microswimmer or ''magic carpet'', finding that for the parameters considered, making the plate wider slowed the swimmer considerably.

The diverse geometries of natural and artificial bodies that interact with microscale flows drives the need for bespoke numerical schemes that can solve hydrodynamic problems efficiently and accurately. By applying a regularised stokeslet method, we have examined the dynamics of ribbons and sheets that will be effective for a range of problems where the body thickness is much smaller than the other dimensions, and may provide a means to couple flows with plate mechanics to study fluid structure interaction problems such as the sedimention of flexible pancake-like structures, or the unfolding of chiral ribbons in ambient flow.

Acknowledgements

TDM-J is supported by a Royal Commision for the Exhibition of 1851 Research Fellowship; L. K. is supported by the Cambridge Trusts, Cambridge Philosophical Society and the Cambridge hardship fund; E. L. is supported in part by the European Union through a Marie Curie CIG Grant.

References

1 S. Kim and S. J. Karrila, *Microhydrodynamics: Principles and Selected Applications*, Courier Corporation, 2005, p. 507.
2 E. Guyon, J.-P. Hulin, L. Petit and C. Mitescu, *Physical Hydrodynamics*, OUP Oxford, 2001, p. 528.
3 L. E. Becker, S. A. Koehler and H. A. Stone, *J. Fluid Mech.*, 2003, **490**, 15–35.
4 E. Lauga and T. R. Powers, *Rep. Prog. Phys.*, 2009, **72**, 096601.
5 G. K. Youngren and A. Acrivos, *J. Fluid Mech.*, 1975, **69**, 377–403.
6 C. Pozrikidis, *Boundary Integral and Singularity Methods for Linearized Viscous Flow*, Cambridge University Press, 1992, p. 259.
7 N. Phan-Thien, T. Tran-Cong and M. Ramia, *J. Fluid Mech.*, 1987, **184**, 533–549.
8 H. Shum, E. Gaffney and D. Smith, *Proc. R. Soc. London, Ser. A*, 2010, 1725–1748.
9 T. D. Montenegro-Johnson and E. Lauga, *Phys. Rev. E: Stat., Nonlinear, Soft Matter Phys.*, 2014, **89**, 060701.
10 T. D. Montenegro-Johnson, D. Gagnon, P. E. Arratia and E. Lauga, *Phys. Rev. Fluids*, 2016, **1**, 053202.
11 G. J. Hancock, *Proc. R. Soc. London, Ser. A*, 1953, pp. 96–121.
12 J. Gray and G. J. Hancock, *J. Exp. Biol.*, 1955, **32**, 802–814.
13 R. G. Cox, *J. Fluid Mech.*, 1970, **44**, 791.
14 G. K. Batchelor, *J. Fluid Mech.*, 1970, **44**, 419.
15 J. Lighthill, *SIAM Rev.*, 1976, **18**, 161–230.
16 R. E. Johnson, *J. Fluid Mech.*, 1979, **99**, 411.
17 L. Koens and E. Lauga, *Phys. Biol.*, 2014, **11**, 1–15.
18 M. Kim and T. Powers, *Phys. Rev. E: Stat., Nonlinear, Soft Matter Phys.*, 2004, **69**, 061910.
19 S. E. Spagnolie and E. Lauga, *Phys. Fluids*, 2010, **22**, 031901.
20 S. E. Spagnolie and E. Lauga, *Phys. Rev. Lett.*, 2011, **106**, 058103.
21 L. Koens and E. Lauga, *Phys. Fluids*, 2016, **28**, 013101.
22 L. Zhang, J. J. Abbott, L. Dong, B. E. Kratochvil, D. Bell and B. J. Nelson, *Appl. Phys. Lett.*, 2009, **94**, 064107.
23 L. Zhang, J. J. Abbott, L. Dong, K. E. Peyer, B. E. Kratochvil, H. Zhang, C. Bergeles and B. J. Nelson, *Nano Lett.*, 2009, **9**, 3663–3667.
24 L. Zhang, K. E. Peyer and B. J. Nelson, *Lab Chip*, 2010, **10**, 2203–2215.
25 E. Diller, J. Zhuang, G. Z. Lum, M. R. Edwards and M. Sitti, *Appl. Phys. Lett.*, 2014, **104**, 174101.
26 B. Gryseels, K. Polman, J. Clerinx and L. Kestens, *Lancet*, 2006, **368**, 1106–1118.
27 D. J. Smith, *Proc. R. Soc. London, Ser. A*, 2009, 3605–3626.
28 E. E. Keaveny and M. J. Shelley, *J. Comput. Phys.*, 2011, **230**, 2141–2159.
29 R. Cortez, L. Fauci and A. Medovikov, *Phys. Fluids*, 2005, **17**, 031504.
30 T. D. Montenegro-Johnson, S. Michelin and E. Lauga, *Eur. Phys. J. E: Soft Matter Biol. Phys.*, 2015, **38**, 1–7.
31 F. Perrin, *J. Phys. Radium*, 1934, **10**, 497–511.
32 P.-O. Persson and G. Strang, *SIAM Rev.*, 2004, **46**, 329–345.
33 E. E. Keaveny, S. W. Walker and M. J. Shelley, *Nano Lett.*, 2013, **13**, 531–537.
34 T. Omori, H. Hosaka, Y. Imai, T. Yamaguchi and T. Ishikawa, *Phys. Rev. E: Stat., Nonlinear, Soft Matter Phys.*, 2014, **89**, 013008.
35 S. D. Olson, S. Lim and R. Cortez, *J. Comput. Phys.*, 2013, **238**, 169–187.
36 G. I. Taylor, *Proc. R. Soc. London, Ser. A*, 1951, 447–461.
37 J. R. Vélez-Cordero and E. Lauga, *J. Non-Newtonian Fluid Mech.*, 2013, **199**, 37–50.
38 E. E. Riley and E. Lauga, *J. Theor. Biol.*, 2015, **382**, 345–355.
39 T. D. Montenegro-Johnson, H. Gadelha and D. J. Smith, *R. Soc. Open Sci.*, 2015, **2**, 140475.